

# Emergent Antipolar Phase in BiFeO<sub>3</sub>–La<sub>0.7</sub>Sr<sub>0.3</sub>MnO<sub>3</sub> Superlattice

Wen Dong,\* Jonathan J. P. Peters, Dorin Rusu, Michael Staniforth, Alan E. Brunier, James Lloyd-Hughes, Ana M. Sanchez, and Marin Alexe\*



Cite This: <https://dx.doi.org/10.1021/acs.nanolett.0c02063>



Read Online

ACCESS |



Metrics & More



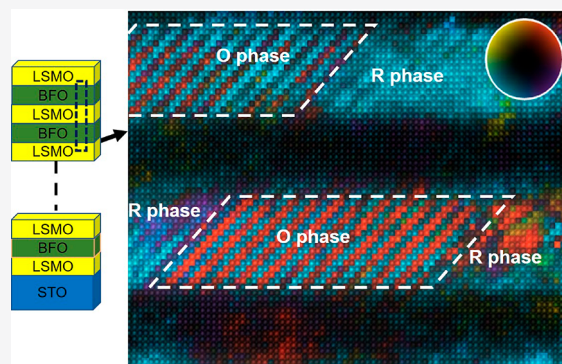
Article Recommendations



Supporting Information

**ABSTRACT:** Ferroelectric–paraelectric superlattices show emerging new states, such as polar vortices, through the interplay and different energy scales of various thermodynamic constraints. By introducing magnetic coupling at BiFeO<sub>3</sub>–La<sub>0.7</sub>Sr<sub>0.3</sub>MnO<sub>3</sub> interfaces epitaxially grown on SrTiO<sub>3</sub> substrate, we find, for the first time in thin films, a sub-nanometer thick lamella-like BiFeO<sub>3</sub>. The emergent phase is characterized by an arrangement of a two unit cell thick lamella-like structure featuring antiparallel polarization, resulting an antiferroelectric-like structure typically associated with a morphotropic phase transition. The antipolar phase is embedded within a nominal R3c structure and is independent of the BiFeO<sub>3</sub> thickness (4–30 unit cells). Moreover, the superlattice structure with the morphotropic phase demonstrates azimuth-independent second harmonic generation responses, indicating a change of overall symmetry mediated by a delicate spatial distribution of the emergent phase. This work enriches the understanding of a metastable state manipulated by thermodynamic constraints by lattice strain and magnetic coupling.

**KEYWORDS:** BiFeO<sub>3</sub>, multiferroic, thin films, strain engineering, spin–charge–lattice coupling



Epitaxial growth of oxide thin films provides the ability to artificially engineer the polar long-range order of the film materials through strain, thickness, interfacial coupling, etc. By tuning the growth conditions, the oxide properties can be enhanced with respect to the bulk counterpart. BiFeO<sub>3</sub> (BFO) constitutes the classical example, with the leakage problems associated with the defective bulk crystal structure being solved using thin films grown by pulsed laser deposition (PLD). Superlattices containing complex oxides have boosted novel phenomena, such as strain-induced ferroelectricity,<sup>1</sup> strong ferroelectric ferromagnets,<sup>2</sup> and, more recently, flux-closure domains,<sup>3</sup> polar vortices,<sup>4,5</sup> and polar skyrmions.<sup>6</sup> These emergent phenomena arise from the interplay between spin, orbital, charge, and lattice degrees of freedom. The variations in energy scales of different thermodynamic constraints such as temperature, magnetic field, electric field, and mechanical strain from epitaxial are powerful variables that can be used to control certain new states. By interface engineering, certain constraints can be formed due to proximity of different materials, and the long-range order of the material can be artificially engineered to give rise to a plethora of physical phenomena.

Interface engineering has unleashed the unprecedented ferrotoroidic structures in a ferroelectric (FE)-based oxide superlattice confined by insulating paraelectric (PE) oxide layers. Taking the FE–PE superlattice structure of PbTiO<sub>3</sub>–SrTiO<sub>3</sub> (PTO–STO) grown on DyScO<sub>3</sub> (DSO) as an example, by increasing the FE layer thickness, the domain structure

moves from classical a1/a2 domains to polar vortices to flux closure domains. This popular structure provides a textbook evolution of different states in relation to the depolarization field superimposed by unscreened ferroelectric-bound charge. However, a similar vortex structure is also stabilized in PTO confined by ferromagnetic (FM) Co and La<sub>0.7</sub>Sr<sub>0.3</sub>MnO<sub>3</sub> (LSMO) electrodes.<sup>7</sup> The FM–FE–FM heterostructure disentangles the interplay between the elastic and electric field in combination with the modulation of spin–lattice coupling, providing the appropriate energy to the vortex structures' stabilization.<sup>7,8</sup> Compared to the PE–FE–PE heterostructure, magnetic coupling will be present at the FM–FE interface. This coupling is generally of a lower energy magnitude compared with that of charge and lattice constraints from the electric field and stress, respectively, that are often considered in superlattice films.<sup>9</sup>

In this work, we focus on the potential phase manipulation from magnetic coupling in superlattices. This magnetic coupling is present in the heterostructures along with the more prominent magnetic coupling and lattice constraints.

**Received:** May 14, 2020

**Revised:** July 7, 2020

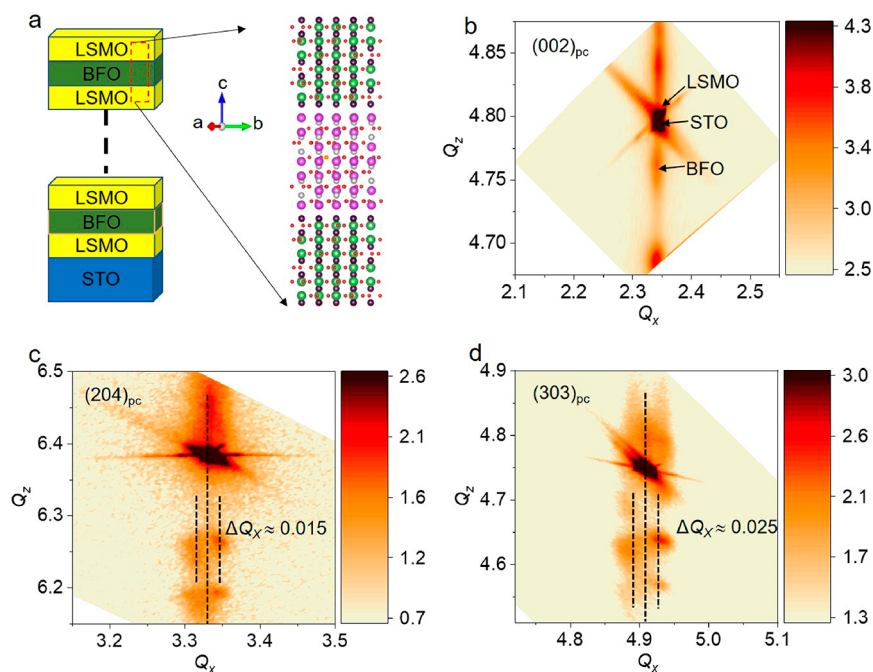


**Figure 1.** (a) Schematic of the designed BFO–LSMO superlattice deposited on STO substrates, where the proximity effect of two interfaces can lead to unexpected properties in the BFO film. (b) X-ray diffraction reciprocal space maps (RSM) around the substrate’s  $(113)_{pc}$  diffraction condition. (c) RSM around the substrate’s  $(204)_{pc}$  diffraction condition. (d) RSM around the substrate’s  $(303)_{pc}$  diffraction condition.

More specifically, short-period (of only a few unit cells) superlattices of BFO–LSMO are shown in Figure 1a, where multiferroic BFO is an antiferromagnetic (AFM) and FE at room temperature and LSMO is FM. The proximity effect of interfaces can lead to unexpected properties in the BFO film. Thus, a canted magnetic state in the antiferromagnetic BFO is suggested to be enhanced at the BFO–LSMO interface.<sup>10,11</sup> Recent studies have shown that ultrathin LSMO is favorable to form/stabilize ferromagnetic order at BFO–LSMO interfaces due to its unconventional polar structure.<sup>8</sup> Moreover, strong orbital hybridization between Fe and Mn across the interfaces would enhance the magnetic coupling in the many-pair superlattice structures.<sup>12</sup>

Our designed superlattices are grown on STO substrates, of the form  $\text{STO-LSMO}_{25 \text{ u.c.}}-(\text{BFO}_{N \text{ u.c.}}-\text{LSMO}_{13 \text{ u.c.}})_M$ , where subscript  $M$  indicates the number of BFO–LSMO pairs and  $N$  gives the number of BFO unit cells (u.c.). Samples in the form of  $\text{STO-LSMO}_{25 \text{ u.c.}}-(\text{BFO}_{N \text{ u.c.}}-\text{LSMO}_{13 \text{ u.c.}})_9$  ( $N$  ranges from 13 to 30) with a demonstrated flat surface (roughness within 400 pm, i.e., less than one u.c., Figure S1) were obtained by PLD. The X-ray diffraction (XRD) reciprocal space maps (RSMs) measured in this heterostructure are shown in Figure 1b–d. These RSMs reveal a high-quality superlattice. Thus, for example, the typical superlattice peaks around the substrate’s  $(113)$  diffraction condition (Figure 1b) suggest that the superlattice growth is coherently strained onto the STO substrate. However, an obvious peak splitting can be observed at higher indices, such as  $(204)$  and  $(303)$  (shown in Figure 1c,d, respectively), which potentially suggests a periodic modulation and Bragg reflections from crystallographic tilted domains. The satellite spacings in the RSMs around  $(204)_{pc}$  and  $(303)_{pc}$  diffraction conditions are  $\Delta Q_x \approx 0.015$  and  $\approx 0.025$ , respectively, which correspond to real space periodicities of 83.776 and 75.398 nm, respectively. The pair of satellite peaks in  $(204)_{pc}$  and  $(303)_{pc}$  obviously have no equal spacing, suggesting a tilting of the crystal structure rather

than a modulation of the periodic domain structure to be the potential reason for the splitting.<sup>13,14</sup>

Using scanning transmission electron microscopy (STEM), the local structure of the superlattices was analyzed. A low-magnification STEM image of the superlattice sample (Figure 2a) taken along the  $[100]$  zone axis reveals the different BFO–LSMO layer pairs as a bright/dark contrast. Figure 2b corresponds to an atomic resolution annular dark-field (ADF) STEM image, with the contrast proportional to the atomic number  $Z$ . Thus, BFO layers appear brighter than LSMO in this type of image. These images also confirm the formation of sharp and coherent interfaces without any dislocation. A striped lamella structure within some areas of the BFO layers can be clearly seen on closer examination of Figure 2b. Each lamella is oriented at  $45^\circ$  from the BFO–LSMO interface with a periodicity of 2 u.c. and an apparent large shift of the Bi atoms. This structure is evident by mapping the  $c/a$  lattice parameter ratio at each unit cell (Figure 2c). The striped lamellae are clearly visible, with a  $c/a$  ratio changing from 1.15 to 0.90 between consecutive lamellae. Regular rhombohedral BFO areas ( $c/a \approx 1.05$ ) are also visible as well as the LSMO with  $c/a \approx 1.00$ . This is further indicated from the strain mapping shown in Figure S2, where the sub-nanoscale lamella profiles are obvious. Mapping of the displacement (Bi respect to the Fe frame) ( $P_{PD}$ ) performed on the lamella structure suggests a totally different polarization behavior compared to that with typical rhombohedral BFO, shown in Figure 2d,e. The typical  $R3c$  BFO structure shows a polarization along  $[111]$  (where the component out of the image plane has to be assumed due to the projection effect in STEM imaging). A higher-magnification image of the displacement mapping in the striped lamellae area (Figure 2e) shows antiferroelectric polarization in the lamellae (i.e., the polarization points in opposite directions for consecutive lamella). Morozovska et al.<sup>15</sup> previously observed a similar structure in  $\text{La}_{0.22}\text{Bi}_{0.78}\text{FeO}_3$  (LBFO) thick films (grown on  $\text{SrRuO}_3$ –

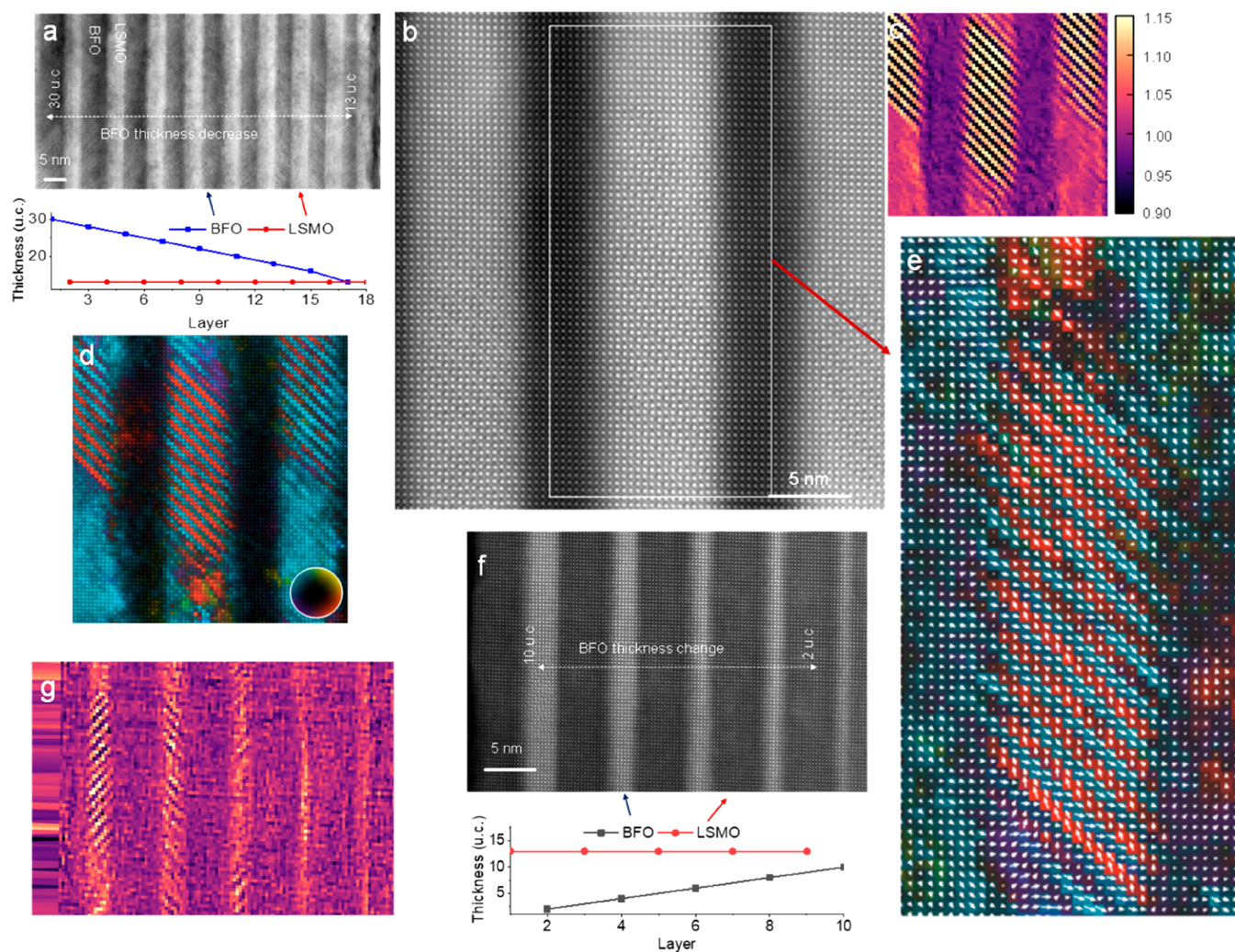


**Figure 2.** (a) Cross-sectional bright-field STEM image of the STO–LSMO<sub>25 u.c.</sub>–(BFO<sub>*N* u.c.</sub>–LSMO<sub>13 u.c.</sub>)<sub>9</sub> (*N* ranges from 13 to 30) superlattice, taken along the [100] zone axis. (b) Atomic resolution ADF image of an area in (a). (c) *c/a* ratio mapping corresponds to (b). (d) Low-magnification polarization mapping corresponds to (b). (e) Higher-magnification displacement mapping of the area enclosed in a white rectangle in (b). (f) Cross-sectional ADF STEM image of the STO–LSMO<sub>25 u.c.</sub>–(BFO<sub>*N* u.c.</sub>–LSMO<sub>13 u.c.</sub>)<sub>5</sub> (*N* ranges from 2 to 10) superlattice. (g) *c/a* ratio mapping corresponds to (e).

STO–Si). The LBFO is close to an orthorhombic–rhombohedral ( $R3c$ – $Pbnm$ ) morphotropic phase boundary (MPB). A similar antiferroelectric structure was also observed in superlattices of BFO–LaFeO<sub>3</sub> (BFO–LFO) by strain engineering<sup>16</sup> and BFO–LBFO grown on TbScO<sub>3</sub> (TSO) substrates by tuning the electrostatic field.<sup>17–19</sup> To determine if the structures observed in Figure 2 are a result of La incorporation in the BFO layers (due to unintentional diffusion from the LSMO layer), energy-dispersive X-ray spectroscopy (EDS) was performed in STEM to provide elemental compositional analysis, along the different BFO–LSMO layers (Figure S3). This EDS profile shows there is negligible La content in the BFO compared with 22% in the LBFO of Morozovska et al.<sup>15</sup>, confirming that the BFO lamellar structure is not an accidental La doping–diffusion process but rather due to epitaxial engineering.

Furthermore, this striped lamella structure is stable for a wide range of film thickness. Figure 2f shows a BFO–LSMO superlattice with the corresponding *c/a* ratio map in Figure 2g. Here, the BFO thickness varies from 2 to 10 u.c., with the striped lamella structure present in BFO films as thin as 4 u.c.

At the other end of the scale, the absence of peak splitting in the RSM pattern of superlattice samples with *N* greater than 32 u.c. (Figure S4) suggests that an upper limit for the formation of the antipolar structure is 32 u.c. This gives a BFO thickness range of 4 to 30 u.c. on LSMO (13 u.c.) to generate this emergent phase. STEM imaging followed by displacement analysis and strain mapping analysis along the [110] direction of the superlattice demonstrates no obvious lamella-like structure. Therefore, there is no alignment of the lamella structure along the [110] direction (Figure S5). By fixing the thickness of BFO in the superlattice (i.e., STO–LSMO<sub>13 u.c.</sub>–(BFO<sub>13 u.c.</sub>–LSMO<sub>13 u.c.</sub>)<sub>13</sub> superlattice with *N* = 13, a similar peak splitting was observed in the RSM pattern. This splitting was obtained in azimuth ( $\phi$ )-dependent measurements ( $\phi$  = 0 and 90°), which confirms the alignment of the lamella structures along both [100] and [010] directions (Figures S6 and S7). For example, in Figure 3a, we provide a simple model to roughly demonstrate and help the understanding of the alignment and the distribution of the striped lamellae. The selected area electron diffraction pattern of the striped lamellae area displays a  $1/4(-h0l)$  reflection (Figure S8) similar to that

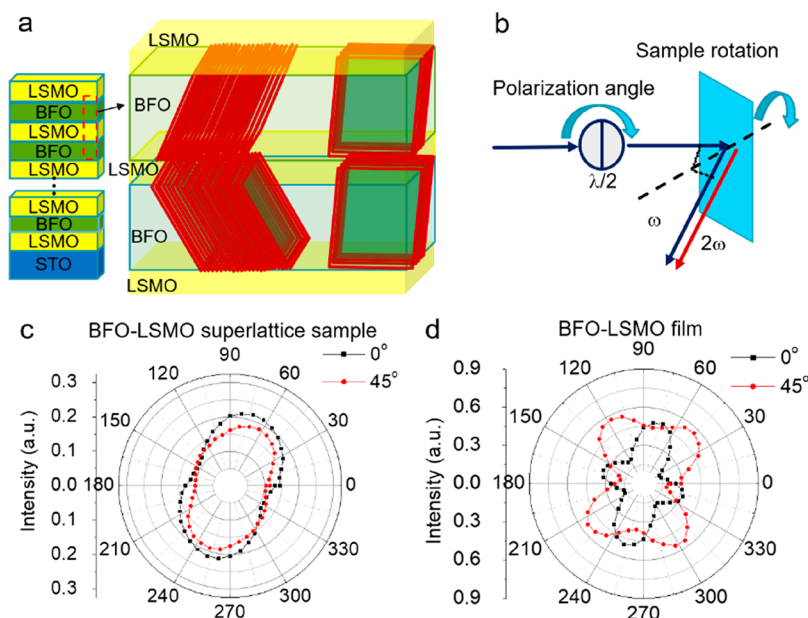


**Figure 3.** (a) Rough simple model of the distribution of the lamella structure along both  $[100]$  and  $[010]$  directions. (b) Schematic diagram of the second harmonic generation (SHG) measurement on  $\text{STO}-\text{LSMO}_{13 \text{ u.c.}}-(\text{BFO}_{13 \text{ u.c.}}-\text{LSMO}_{13 \text{ u.c.}})_{13}$  superlattice. (c) SHG polar plots obtained from the BFO–LSMO superlattice sample without (black) and with (red)  $45^\circ$  clockwise rotation. (d) SHG polar plots obtained from the normal BFO–LSMO multilayer sample without (black) and with (red)  $45^\circ$  clockwise rotation.

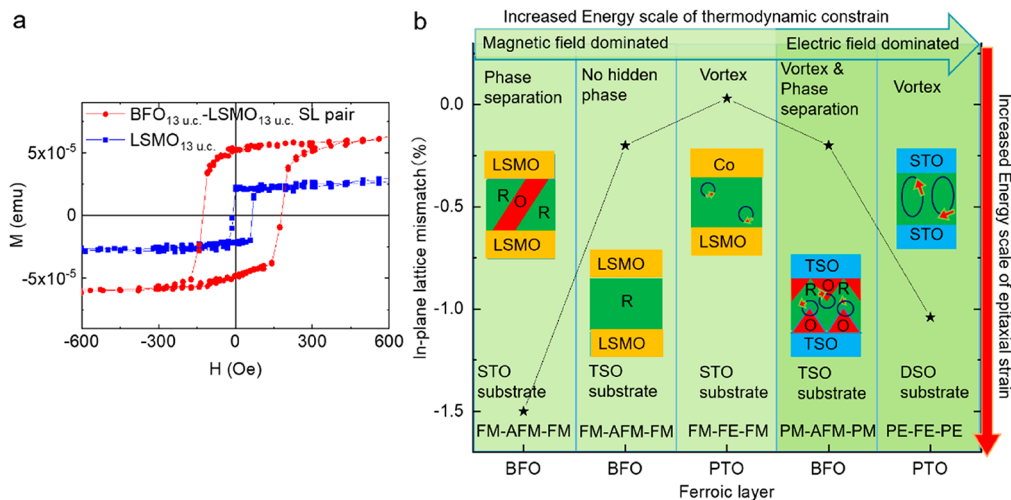


**Figure 4.** (a) Magnetic hysteresis behavior of the pure LSMO and superlattice (SL) sample  $\text{STO}-\text{LSMO}_{13 \text{ u.c.}}-(\text{BFO}_{13 \text{ u.c.}}-\text{LSMO}_{13 \text{ u.c.}})_{13}$  measured at 10 K. The magnetization of the superlattice sample was extracted to each  $\text{BFO}_{13 \text{ u.c.}}-\text{LSMO}_{13 \text{ u.c.}}$  superlattice pair. (b) Rough diagram of the evolution of hidden phases in a ferroic layer by thermodynamic constraints (i.e., including epitaxial strain, magnetic field, electric field) with different energy scales based on experimental results and reported literature. The ferroic layers were typically exemplified by BFO and PTO. Different substrates, including STO,  $\text{TbScO}_3$  (TSO), and  $\text{DyScO}_3$  (DSO), provide the mismatch variations. R and O indicate the rhombohedra and orthorhombus, respectively.

found in an antiferroelectric (AFE) orthorhombic  $\text{PbZrO}_3$ -like structure.<sup>20</sup> The superlattice reflection indicates a quadrupling of the pseudocubic unit cell with the periodicity of  $\sim 11.3 \text{ \AA}$ , which is the same as the  $1/4(-101)$  reflections in  $\text{LBFO}-\text{SrRuO}_3-\text{STO}-\text{Si}$ .<sup>15</sup>

To learn more about the structure and functional properties of the new phase, the symmetry of the BFO layer was investigated by nonlinear optical second harmonic generation (SHG) for its domain symmetry-sensitive ability. The SHG measurement setup is in a reflection mode, as shown in Figure 3b with an 800 nm fundamental beam. The SHG experiments were performed on a  $\text{STO}-\text{LSMO}_{25 \text{ u.c.}}-(\text{BFO}_{13 \text{ u.c.}}-$

$\text{LSMO}_{13 \text{ u.c.}})_{13}$  superlattice structure and  $\text{STO}-\text{LSMO}_{25 \text{ u.c.}}-\text{BFO}_{35 \text{ nm}}$  film (without superlattice) for comparison. Samples were rotated around the  $[001]$  direction in the SHG experiments. The superlattice sample, with the emergent antiferroelectric-like structure, shows overall two-fold rotational symmetry (Figure 3c) with near azimuthal independence between  $0$  and  $45^\circ$  angles of an oriented sample. In contrast, the  $\text{STO}-\text{LSMO}_{25 \text{ u.c.}}-\text{BFO}_{35 \text{ nm}}$  system (Figure 3d) shows the expected four-fold rotational symmetry corresponding to the rhombohedral BFO structure,<sup>21</sup> and its SHG signal strictly rotates by  $45^\circ$  when the sample is rotated by  $45^\circ$ . One should note that the normal BFO–LSMO structure in the comparison

sample shows four-fold symmetry similar to other SHG observations from the R3c ferroelectric structure.<sup>22</sup> There is no obvious effect from the ferromagnetic LSMO on the SHG signal of the BFO. In the superlattice sample, the coexistence of the new phase with an antipolar structure significantly changes to a two-fold-like symmetry. Principally, the new antipolar phase should produce no SHG signal and the normal BFO area should still show four-fold symmetry. Considering the negligible effect from the LSMO as indicated the comparison BFO–LSMO measurements, it would be reasonable to think that the new antipolar phase should be mainly responsible for lowering the symmetry of the superlattice sample. The distinct two-fold rotational symmetry in the superlattice structure with nearly isotropic SHG response relative to the rotation of the sample around [001] axis suggests that the superstructure and its spatial distribution have totally changed the macroscopic SHG response and polarization behavior of the BFO layer. The near azimuth-independent SHG signal challenges our conventional understanding of the SHG response relative to the symmetry and polarization of the materials, which need further detailed research.

In addition to the abnormal SHG response, magnetic hysteresis in the LSMO–BFO superlattice at 10 K is shown in Figure 4a, compared with the just one LSMO layer, suggesting an enhanced ferromagnetism in the superlattice due to magnetic coupling at the AFM–FM interface as previously reported.<sup>12</sup> One should note that there is a high in-plane lattice mismatch of  $-1.4\%$  between the STO substrates and BFO bulk. We also checked the LSMO–BFO superlattice structure grown on TSO with  $\sim 5$  nm and  $\sim 8$  nm thick BFO. In this case, BFO ( $-0.2\%$  strain) shows no observable peak splitting in RSM scanning, indicating no tilted or topological textures (Figures S9 and S10). Therefore, the lattice mismatch induced strain should be the key driver, whereas the magnetic coupling should also be responsible for the appearance of the antiferroelectric-like phase in the BFO–LSMO superlattice.

Figure 4b shows the evolution of hidden phases in ferroic layers manipulated by thermodynamic constraints (i.e., magnetic field, electric field, and lattice strain), based on our experimental results and reported literature. For FE–PE superlattice structures, such as ferroic layers (i.e., PTO, BFO) confined by insulating layers (i.e., STO, TSO), they provide large scales of energy (electric field) to manipulate the ground states and lead to emergent topologically protected vortex phases.<sup>3,4,7,8,23,24</sup> For FM–AFM superlattice structures, the low energy constraint from the magnetic field by metallic FM structure is more likely to give rise to separate phases, especially at high lattice mismatch/strain. The phase separation is also observed in BFO confined with an insulating AFM LFO layer, in which case the strain and electrostatic force are suggested to be responsible for the phase separation.<sup>16</sup> However, FM–FE superlattice structures, such as the PTO confined by the metallic FM layer, can also give rise to vortex structures. Even in the BFO constrained by TSO, the vortex structure coexists with separation of O and R phases.<sup>23,24</sup> Therefore, in our case, the magnetic coupling and the AFM nature of the BFO layer are responsible alongside the main contribution from epitaxial strain for the inability to give rise to the topological textures like those observed in the PTO–STO.

In conclusion, we obtained insight into the understanding of a hidden phase in epitaxially strained ferroic layers with additional constraints by the magnetic field coupling at the low

end of the energy scale of thermodynamic variables. By growing a BFO–LSMO superlattice on STO substrates, we obtained a highly strained orthorhombic phase within the BFO layer with aligned sub-nanometer thick lamella-like structures coexisting with the normal pseudorhombohedral BFO phase. The lamellae are parallel to the (101) or (011) plane with  $a/c$  ratio changing from 1.15 to 0.90 between consecutive lamella. STEM analysis also suggests a similar electron diffraction pattern of  $1/4(101)$  reflections arising from orthorhombic-like structure claimed only in LBFO with O and R MPB composition or highly strained BFO grown on orthorhombic substrates but only close to the substrate due to the proximity effect. Moreover, nearly azimuth-independent SHG responses relative to the rotation of the sample around the [001] axis suggest a delicate spatial distribution of the superstructure in the BFO layer, which changes the overall polarization behavior and symmetry of the BFO layer. Compared with the topologically protected hidden phase in ferroic layers powerfully constrained by electric fields, it is found that the antiferromagnetic BFO layer confined by ferromagnetic LSMO at the metallic boundary conditions more easily experiences a phase separation. Apart from the epitaxial strain being the key driver for the appearance of the new phase, the phase separation should be also related to the FM–AFM coupling. The superstructure in the BFO epitaxially confined by the ferromagnetic LSMO layer may show intriguing electronic transport properties, such as in the form of a multiferroic tunnel junction.

## ■ ASSOCIATED CONTENT

### Supporting Information

The Supporting Information is available free of charge at <https://pubs.acs.org/doi/10.1021/acs.nanolett.0c02063>.

Methods and supporting figures (PDF)

## ■ AUTHOR INFORMATION

### Corresponding Authors

Wen Dong – Department of Physics, University of Warwick, Coventry CV4 7AL, United Kingdom; [orcid.org/0000-0001-7242-7239](https://orcid.org/0000-0001-7242-7239); Email: [albert\\_d\\_w@hotmail.com](mailto:albert_d_w@hotmail.com)

Marin Alexe – Department of Physics, University of Warwick, Coventry CV4 7AL, United Kingdom; [orcid.org/0000-0002-0386-3026](https://orcid.org/0000-0002-0386-3026); Email: [m.alex@warwick.ac.uk](mailto:m.alex@warwick.ac.uk)

### Authors

Jonathan J. P. Peters – Department of Physics, University of Warwick, Coventry CV4 7AL, United Kingdom; [orcid.org/0000-0001-6858-7037](https://orcid.org/0000-0001-6858-7037)

Dorin Rusu – Department of Physics, University of Warwick, Coventry CV4 7AL, United Kingdom

Michael Staniforth – Department of Physics, University of Warwick, Coventry CV4 7AL, United Kingdom

Alan E. Brunier – Department of Physics, University of Warwick, Coventry CV4 7AL, United Kingdom

James Lloyd-Hughes – Department of Physics, University of Warwick, Coventry CV4 7AL, United Kingdom; [orcid.org/0000-0002-9680-0138](https://orcid.org/0000-0002-9680-0138)

Ana M. Sanchez – Department of Physics, University of Warwick, Coventry CV4 7AL, United Kingdom; [orcid.org/0000-0002-8230-6059](https://orcid.org/0000-0002-8230-6059)

Complete contact information is available at: <https://pubs.acs.org/10.1021/acs.nanolett.0c02063>

## Notes

The authors declare no competing financial interest.

## ACKNOWLEDGMENTS

The work was partly supported by the EPSRC (U.K.) through Grant Nos. EP/M022706/1, EP/P031544/1, and EP/P025803/1. M.A. acknowledges the Wolfson Research Merit and Theo Murphy Blue-sky Awards of Royal Society.

## REFERENCES

- (1) Haeni, J. H.; Irvin, P.; Chang, W.; Uecker, R.; Reiche, P.; Li, Y. L.; Choudhury, S.; Tian, W.; Hawley, M. E.; Craigo, B.; Tagantsev, A. K.; Pan, X. Q.; Streiffer, S. K.; Chen, L. Q.; Kirchoefer, S. W.; Levy, J.; Schlom, D. G. Room-temperature ferroelectricity in strained SrTiO<sub>3</sub>. *Nature* **2004**, *430* (7001), 758–761.
- (2) Lee, J. H.; Fang, L.; Vlahos, E.; Ke, X.; Jung, Y. W.; Kourkoutis, L. F.; Kim, J.-W.; Ryan, P. J.; Heeg, T.; Roeckerath, M.; Goian, V.; Bernhagen, M.; Uecker, R.; Hammel, P. C.; Rabe, K. M.; Kamba, S.; Schubert, J.; Freeland, J. W.; Muller, D. A.; Fennie, C. J.; Schiffer, P.; Gopalan, V.; Johnston-Halperin, E.; Schlom, D. G. A strong ferroelectric ferromagnet created by means of spin–lattice coupling. *Nature* **2010**, *466* (7309), 954–958.
- (3) Tang, Y. L.; Zhu, Y. L.; Ma, X. L.; Borisevich, A. Y.; Morozovska, A. N.; Eliseev, E. A.; Wang, W. Y.; Wang, Y. J.; Xu, Y. B.; Zhang, Z. D.; Pennycook, S. J. Observation of a periodic array of flux-closure quadrants in strained ferroelectric PbTiO<sub>3</sub> films. *Science* **2015**, *348* (6234), 547–551.
- (4) Yadav, A. K.; Nelson, C. T.; Hsu, S. L.; Hong, Z.; Clarkson, J. D.; Schleputz, C. M.; Damodaran, A. R.; Shafer, P.; Arenholz, E.; Dedon, L. R.; Chen, D.; Vishwanath, A.; Minor, A. M.; Chen, L. Q.; Scott, J. F.; Martin, L. W.; Ramesh, R. Observation of polar vortices in oxide superlattices. *Nature* **2016**, *530* (7589), 198–201.
- (5) Damodaran, A. R.; Clarkson, J. D.; Hong, Z.; Liu, H.; Yadav, A. K.; Nelson, C. T.; Hsu, S. L.; McCarter, M. R.; Park, K. D.; Kravtsov, V.; Farhan, A.; Dong, Y.; Cai, Z.; Zhou, H.; Aguado-Puente, P.; García-Fernández, P.; Íñiguez, J.; Junquera, J.; Scholl, A.; Raschke, M. B.; Chen, L. Q.; Fong, D. D.; Ramesh, R.; Martin, L. W. Phase coexistence and electric-field control of toroidal order in oxide superlattices. *Nat. Mater.* **2017**, *16*, 1003.
- (6) Das, S.; Tang, Y. L.; Hong, Z.; Gonçalves, M. A. P.; McCarter, M. R.; Klewe, C.; Nguyen, K. X.; Gómez-Ortiz, F.; Shafer, P.; Arenholz, E.; Stoica, V. A.; Hsu, S. L.; Wang, B.; Ophus, C.; Liu, J. F.; Nelson, C. T.; Saremi, S.; Prasad, B.; Mei, A. B.; Schlom, D. G.; Íñiguez, J.; García-Fernández, P.; Muller, D. A.; Chen, L. Q.; Junquera, J.; Martin, L. W.; Ramesh, R. Observation of room-temperature polar skyrmions. *Nature* **2019**, *568* (7752), 368–372.
- (7) Peters, J. J. P.; Apachitei, G.; Beanland, R.; Alexe, M.; Sanchez, A. M. Polarization curling and flux closures in multiferroic tunnel junctions. *Nat. Commun.* **2016**, *7*, 13484.
- (8) Guo, H.; Wang, Z.; Dong, S.; Ghosh, S.; Saghayezhian, M.; Chen, L.; Weng, Y.; Herklotz, A.; Ward, T. Z.; Jin, R.; Pantelides, S. T.; Zhu, Y.; Zhang, J.; Plummer, E. W. Interface-induced multiferroism by design in complex oxide superlattices. *Proc. Natl. Acad. Sci. U. S. A.* **2017**, *201706814*.
- (9) Ramesh, R.; Schlom, D. G. Creating emergent phenomena in oxide superlattices. *Nat. Rev. Mater.* **2019**, *4*, 257–268.
- (10) Wu, S. M.; Cybart, S. A.; Yu, P.; Rossell, M. D.; Zhang, J. X.; Ramesh, R.; Dynes, R. C. Reversible electric control of exchange bias in a multiferroic field-effect device. *Nat. Mater.* **2010**, *9* (9), 756–761.
- (11) Yu, P.; Lee, J. S.; Okamoto, S.; Rossell, M. D.; Huijben, M.; Yang, C. H.; He, Q.; Zhang, J. X.; Yang, S. Y.; Lee, M. J.; Ramasse, Q. M.; Erni, R.; Chu, Y. H.; Arena, D. A.; Kao, C. C.; Martin, L. W.; Ramesh, R. Interface Ferromagnetism and Orbital Reconstruction in BiFeO<sub>3</sub>-La<sub>0.7</sub>Sr<sub>0.3</sub>MnO<sub>3</sub> Heterostructures. *Phys. Rev. Lett.* **2010**, *105* (2), No. 027201.
- (12) Guo, E.-J.; Petrie, J. R.; Roldan, M. A.; Li, Q.; Desautels, R. D.; Charlton, T.; Herklotz, A.; Nichols, J.; van Lierop, J.; Freeland, J. W.; Kalinin, S. V.; Lee, H. N.; Fitzsimmons, M. R. Spatially Resolved Large Magnetization in Ultrathin BiFeO<sub>3</sub>. *Adv. Mater.* **2017**, *29* (32), 1700790.
- (13) Luo, Z.; Chen, Z.; Yang, Y.; Liu, H.-J.; Huang, C.; Huang, H.; Wang, H.; Yang, M.-M.; Hu, C.; Pan, G.; Wen, W.; Li, X.; He, Q.; Sritharan, T.; Chu, Y.-H.; Chen, L.; Gao, C. Periodic elastic nanodomains in ultrathin tetragonal-like BiFeO<sub>3</sub> films. *Phys. Rev. B: Condens. Matter Mater. Phys.* **2013**, *88* (6), No. 064103.
- (14) Santiso, J.; Balcells, L.; Konstantinovic, Z.; Roqueta, J.; Ferrer, P.; Pomar, A.; Martínez, B.; Sandiumenge, F. Thickness evolution of the twin structure and shear strain in LSMO films. *CrystEngComm* **2013**, *15* (19), 3908–3918.
- (15) Morozovska, A. N.; Eliseev, E. A.; Chen, D.; Nelson, C. T.; Kalinin, S. V. Building a free-energy functional from atomically resolved imaging: Atomic-scale phenomena in La-doped BiFeO<sub>3</sub>. *Phys. Rev. B: Condens. Matter Mater. Phys.* **2019**, *99* (19), 195440.
- (16) Carcan, B.; Bouyanfif, H.; El Marssi, M.; Le Marrec, F.; Dupont, L.; Davoisne, C.; Wolfman, J.; Arnold, D. C. Phase Diagram of BiFeO<sub>3</sub>/LaFeO<sub>3</sub> Superlattices: Antiferroelectric-Like State Stability Arising from Strain Effects and Symmetry Mismatch at Hetero-interfaces. *Adv. Mater. Interfaces* **2017**, *4* (11), 1601036.
- (17) Mundy, J. A.; Heikes, C. A.; Grosso, B. F.; Segedin, D. F.; Wang, Z.; Goodge, B. H.; Meier, Q. N.; Nelson, C. T.; Prasad, B.; Kourkoutis, L. F. A high-energy density antiferroelectric made by interfacial electrostatic engineering. *arXiv* **2018**, <https://arxiv.org/abs/1812.09615?context=cond-mat> (accessed 2020-06-30).
- (18) Graf, M.; Sepliarsky, M.; Tinte, S.; Stachiotti, M. G. Phase transitions and antiferroelectricity in BiFeO<sub>3</sub> from atomic-level simulations. *Phys. Rev. B: Condens. Matter Mater. Phys.* **2014**, *90* (18), 184108.
- (19) Stengel, M.; Íñiguez, J. Electrical phase diagram of bulk BiFeO<sub>3</sub>. *Phys. Rev. B: Condens. Matter Mater. Phys.* **2015**, *92* (23), 235148.
- (20) Woodward, D. L.; Knudsen, J.; Reaney, I. M. Review of crystal and domain structures in the PbZr<sub>x</sub>Ti<sub>1-x</sub>O<sub>3</sub> solid solution. *Phys. Rev. B: Condens. Matter Mater. Phys.* **2005**, *72* (10), 104110.
- (21) Nordlander, J.; De Luca, G.; Strkalj, N.; Fiebig, M.; Trassin, M. Probing Ferroic States in Oxide Thin Films Using Optical Second Harmonic Generation. *Appl. Sci.* **2018**, *8* (4), 570.
- (22) Zhang, Y.; Zhang, Y.; Guo, Q.; Zhong, X.; Chu, Y.; Lu, H.; Zhong, G.; Jiang, J.; Tan, C.; Liao, M.; Lu, Z.; Zhang, D.; Wang, J.; Yuan, J.; Zhou, Y. Characterization of domain distributions by second harmonic generation in ferroelectrics. *npj Comput. Mater.* **2018**, *4* (1), 39.
- (23) Geng, W.; Guo, X.; Zhu, Y.; Tang, Y.; Feng, Y.; Zou, M.; Wang, Y.; Han, M.; Ma, J.; Wu, B.; Hu, W.; Ma, X. Rhombohedral–Orthorhombic Ferroelectric Morphotropic Phase Boundary Associated with a Polar Vortex in BiFeO<sub>3</sub> Films. *ACS Nano* **2018**, *12* (11), 11098–11105.
- (24) Mei, A. B.; Ramesh, R.; Schlom, D. G. Discovery of Ordered Vortex Phase in Multiferroic Oxide Superlattices. *arXiv* **2018**, <https://arxiv.org/abs/1810.12895v1> (accessed 2020-06-30).